PAPER

Loading of Zn/ZnO particles in the precursor feedstock affects the characteristics of liquid plasma sprayed nano-ZnO coatings for photocatalytic applications

View the article online for updates and enhancements.

IOP ebooks™

Bringing together innovative digital publishing with leading authors from the global scientific community.

Start exploring the collection–download the first chapter of every title for free.

Loading of Zn/ZnO particles in the precursor feedstock affects the characteristics of liquid plasma sprayed nano-ZnO coatings for photocatalytic applications

Kuan Chen[1,2], Yi Liu[1,2,5] , Yaoyao Fu[1,2], Jing Huang[1,2], Xiaohua Feng[1,2], Jiang Wang[3], Mengjiao Zhai[1,2], Rocco Lupoi[4], Shuo Yin[4] and Hua Li[1,2,5]

[1] Key Laboratory of Marine Materials and Related Technologies, Zhejiang Key Laboratory of Marine Materials and Protective Technologies, Ningbo Institute of Materials Technology and Engineering, Chinese Academy of Sciences, Ningbo 315201, People's Republic of China
[2] Cixi Institute of Biomedical Engineering, Ningbo Institute of Materials Technology and Engineering, Chinese Academy of Sciences, Ningbo 315201, People's Republic of China
[3] State Key Laboratory of Advanced Special Steels & Shanghai Key Laboratory of Advanced Ferrometallurgy & School of Materials Science and Engineering, Shanghai University, Shanghai 200072, People's Republic of China
[4] Trinity College Dublin, The University of Dublin, Department of Mechanical and Manufacturing Engineering, Parsons Building, Dublin 2, Ireland

E-mail: liuyi@nimte.ac.cn and lihua@nimte.ac.cn

Abstract

It is known that ZnO is an n-type semiconductor with photocatalytic performances under ultraviolet light irradiation. Constructing a superior structure for a modified electron band has been one of the major research goals for photocatalytic ZnO. Here we report a new technical route for making nano-ZnO coatings with a porous topographic morphology. The coatings were fabricated by plasma spraying the mixture of suspension and solution liquid precursors. Pre-loading of ZnO and Zn powders in the precursor was carried out for the purpose of tailoring the structure of the coatings. The coatings in micron thicknesses showed a porous skeleton and a fluffy top layer consisting of ultrafine ZnO grains. Photocatalytic testing by measuring the degradation of methylene blue revealed significantly enhanced activities of the coatings deposited using the ZnO/Zn loaded precursor. The hybrid-structured ZnO coatings exhibited a narrowed band gap and modified oxygen defects as compared to those deposited from the single liquid feedstock. The results shed light on a one-step easy thermal spray fabrication of polytropic nanostructured functional coatings by employing solid powder-loaded liquid as the starting feedstock.

Keywords: nano zinc oxide, liquid plasma spray, ZnO/Zn loaded precursor, photocatalytic activity, oxygen defect

(Some figures may appear in colour only in the online journal)

1. Introduction

Zinc oxide (ZnO) is a well-studied metal oxide with extensive applications in optoelectronics, sensors, biomedicine, and the pharmaceutical industry [1]. It is a wide band gap n-type semiconductor with a high excitation energy (60 mV), giving it the ability to sustain large electric fields and stable optical transmission [2]. In practical industrial production, diverse ZnO with specific features was developed in the form of film or coating, rather than powder or bulk [3–7]. For instance,

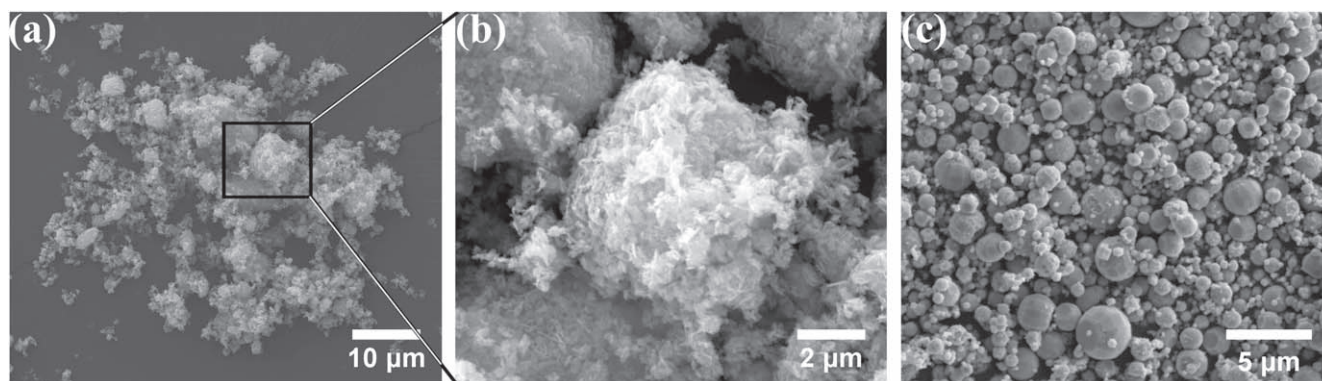[5] Authors to whom any correspondence should be addressed.

Figure 1. Morphology of the nano zinc oxide powder (a), (b) and the zinc powder (c) used for the preparation of the suspension.

ZnO can serve as a photocatalyst under light irradiation to deal with waste water contaminated by organic compounds or heavy metal ions [8–12]. The use of a ZnO as surface coating has shown the competence of the catalyst's recycling ability [10, 11, 13, 14]. The high efficiency of a photocatalytic degradation reaction could be obtained by optimizing the design of the photocatalytic reactor and no by-products would be generated owing to the ecofriendly mineralization of pollutants [15]. The microstructural features of ZnO coatings are therefore critical for their photocatalytic activities.

The microstructural characteristics of ZnO coating, such as grain size, crystallite orientation, and resistivity, are predominately determined by the fabrication techniques [16–18]. ZnO coatings have been prepared by a variety of routes, such as chemical vapor deposition [19], physical vapor deposition [20], atomic layer deposition [21], the sol-gel technique [22], and spray pyrolysis [23]. There are urgent requirements for a fast and feasible one-step deposition technique for making ZnO coatings with appropriate microstructures for advanced photocatalytic performance.

Thermal spray is known for its ease of mass production of surface coatings and simplicity of constructing desired complex coating structures. However, spraying nano-ZnO coatings from pre-synthesized powder usually includes difficulties in controlling their structures, since the microstructure of the coatings is strictly restricted by the shape and size of the starting ZnO powder [24–26]. The splat-packed lamellar structure of thermal sprayed coatings presumably limits their functional applications, since in most cases a large specific surface area is essentially required for the coatings. A liquid plasma spraying process, for instance suspension plasma spray (SPS) and solution precursor plasma spray (SPPS), is a promising route for fabricating coatings with high throughput and good control over their microstructures [27]. Specific coating microstructures can be anticipated as a solution or suspension is used as the feedstock for thermal spraying, from which tuned nanostructures can be obtained through a series of physical and chemical reactions or *in situ* synthesis [28]. Compared with SPS, SPPS is more efficient in the one-step synthesis of nanostructured coatings [29]. Some studies have shown tailored coating structures by altering the starting liquid feedstock or optimizing the spray parameters [30–34].

SPPS allows making a thin coating thickness per pass and successive spraying can cause grain coarsening, which effectively limits the growth of a vertical structure. Zhang *et al* reported SPPS as a novel approach to making a nanostructured ZnO coating with oxygen defects for gas sensing applications [35–37], and Yu *et al* tried a hybrid technical route to fabricate ZnO nanorods and nanowires [38–40]. Yet there are few studies available on fabricating thick porous ZnO coatings for functional applications.

Porous coating nanostructures were fabricated in our previous studies by using adequate additives in the liquid feedstock [41–43]. In this study, we propose a new method to make ZnO coatings with novel structures by combining a well-dispersed suspension with a solution precursor as the spraying feedstock. Nano-ZnO or Zn particles were loaded in the hybrid liquid for the spraying. The chemistry and microstructure of the as-sprayed coatings are examined and their influence on photocatalytic properties is also assessed and elucidated.

2. Materials and methods

Zinc acetate dihydrate (Aladdin Reagent Corporation, China) solution with a concentration of $0.5\,\mathrm{mol\,l^{-1}}$ was prepared as the solution precursor (liquid B: ZnO-SPPS), while equal proportions of deionized water and ethyl alcohol were mixed as the solvent. Before the homogenization of the solution, an adequate amount of acetate acid was added into the hybrid solvent to avoid hydrolysis. Nano zinc oxide powder ($30 \pm 10\,\mathrm{nm}$) or zinc powder ($100\,\mathrm{nm}$), as shown in figure 1, was dispersed in the solvent (liquid A: ZnO-SPS, $40\,\mathrm{g\,l^{-1}}$) or the as-prepared solution (liquid C: ZnO–ZnO, liquid D: ZnO–Zn, $8\,\mathrm{g\,l^{-1}}$) through magnetic stirring and ultrasonic treatment. To acquire steady suspension, polyethylene glycol (PEG-400) and polyvinylpyrrolidone (PVP) were added as the surfactant and binder with a pre-concentration of 20 and 10 wt%, respectively. Prior to the fabrication of the coatings, the substrate 316L stainless-steel plates with the dimension of $20 \times 20 \times 2\,\mathrm{mm}$ were pre-treated by degreasing and sandblasting using 30 mesh corundum and 0.7 MPa compressed air.

Table 1. Plasma spray parameters.

Parameter	Measure
Standoff distance	80 mm
Traverse speed	0.4 m s^{-1}
Primary gas (Ar)	$0.75 \text{ MPa}, 2300 \text{ m}^3 \text{ h}^{-1}$
Secondary gas (H_2)	$0.35 \text{ MPa}, 12 \text{ m}^3 \text{ h}^{-1}$
Net energy	25 kW
Liquid feed rate (ml min^{-1})	100

For the spraying processing, a plasma gun (XM-80SK, Xiuma Spraying Machinery Co. Ltd, Shanghai, China) was fixed with a six-axis robot. A homemade radial liquid feedstock was integrated from a peristaltic pump and stainless-steel needles with an inner diameter of 0.3 mm. During the spraying, the liquid was delivered 2 mm away from the gun exit into the downstream of the plasma torch. The spray parameters are listed in table 1.

The phase composition of the as-sprayed coatings was analyzed by x-ray diffraction (XRD; D8 Advance, Bruker AXS, Germany) using Cu K$_\alpha$ radiation ($\lambda = 1.5406 \text{ Å}$) operated at 40 kV and 40 mA with a scan rate of $0.1°/\text{s}$ over a 2θ range of $10-90°$. The organic component retained in the coatings was characterized by Fourier transformed infrared spectroscopy (FTIR; Nicolet 6700, Thermo Fisher Scientific, USA) with a resolution of 4 cm^{-1} and a scan range of $4000-400 \text{ cm}^{-1}$. The microstructure of the powder and the coatings was examined using a field emission scanning electron microscope (FEG Quanta FEG 250, the Netherlands). To evaluate the light absorption range of the coatings, ultraviolet–visible (UV–vis) diffuse reflectance spectra (DRS) was recorded on a Lambda 950 spectrophotometer (PerkinElmer, USA) using $BaSO_4$ as the reference. As a direct band gap semiconductor, the optical energy gap of ZnO can be acquired from a Tauc plot, which follows the equation $\alpha h\nu = A(h\nu - Eg)^n$, where α is the absorption coefficient, $h\nu$ is the photon energy, A is a constant, Eg is the optical band gap, and n is chosen as $1/2$ for a direct semiconductor [44]. Photoluminescence spectroscopy (PL; with He-Cd 325 nm laser) was utilized to detect the donor defects in the coatings.

The photocatalytic performances of the as-sprayed coatings were evaluated by measuring the degradation of methylene blue under irradiation of both UV light (Philips, TL-D, $\lambda = 365 \text{ nm}$) and artificial sunlight (Xe lamp, GXZ500). The power of the UV light and artificial sunlight are 18 W and 500 W, respectively. For the testing, the samples were immersed in 15 ml of methylene blue solution (5 ppm) contained in a cold trap, while the lamp was placed 15 cm above it. Under magnetic stirring, the whole reaction system was kept in the dark for 1 h to reach an adsorption-desorption equilibrium. Subsequently the degradation process was monitored at a 1 h illumination interval by measuring the absorption intensity using a UV–vis spectrophotometer (MAPADA, UV-3300) operated with an absorbance wavelength of 664 nm.
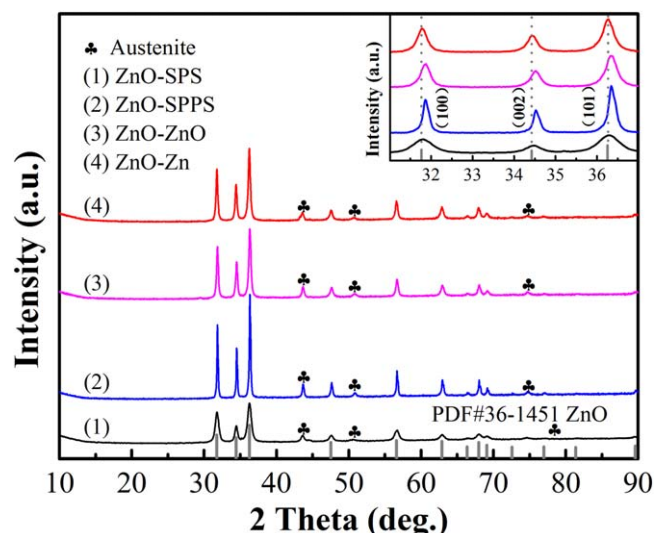

Figure 2. XRD patterns of the ZnO coatings deposited on the 316L substrate (the inset shows the XRD peaks of the ZnO crystal planes (100), (002), and (010)).

3. Results and discussion

The coated ZnO-SPS, ZnO-SPPS, ZnO–ZnO, and ZnO–Zn were fabricated from ZnO suspension, zinc acetate dihydrate solution, zinc acetate dihydrate-ZnO suspension, and zinc acetate dihydrate-Zn suspension, respectively. For the liquid precursor using plasma spraying, different organic additives were selected for homogenization and stabilization of the liquid, which resulted in variable coating structures. As revealed from the XRD patterns shown in figure 2, all the diffraction peaks are indexed as a wurtzite structure of ZnO (JCPDS#36-1451), and no obvious peaks ascribable to impurity and contaminants were detected except for the austenite phase of the 316L substrate. The suspension plasma sprayed coating (ZnO-SPS) showed a broadened curve with the weakest peak intensity, suggesting the retention of the initial nano-ZnO powder. On the contrary, the solution precursor plasma sprayed coatings showed the highest narrowed peak, illustrating well crystallinity of ZnO grains. Furthermore, the coatings deposited using a hybrid feedstock showed similar XRD patterns. It is noted that there was no remaining zinc in the ZnO–Zn coatings. This is likely due to significant metallic oxidation during the high temperature processing. Further crystallographic structural information was also suggested by the position of the three main peaks (figure 2). The ZnO-SPS coating and the ZnO–Zn coating exhibited peaks located at $31.73°$, $34.36°$, and $36.21°$, corresponding to the (100), (002), and (101) planes, respectively. While the other samples showed peak shifting toward higher 2θ angles. According to the Bragg equation, a higher 2θ means smaller d-spacing, which may be triggered by residual stresses or crystalline defects such as vacancies. There is no doubt that the good crystalline structure of the ZnO-SPS coatings was derived from the starting ZnO powder. Surprisingly, regardless of the similarity in liquid feedstock, the ZnO–Zn coating containing the oxidized zinc showed minor or almost no peak
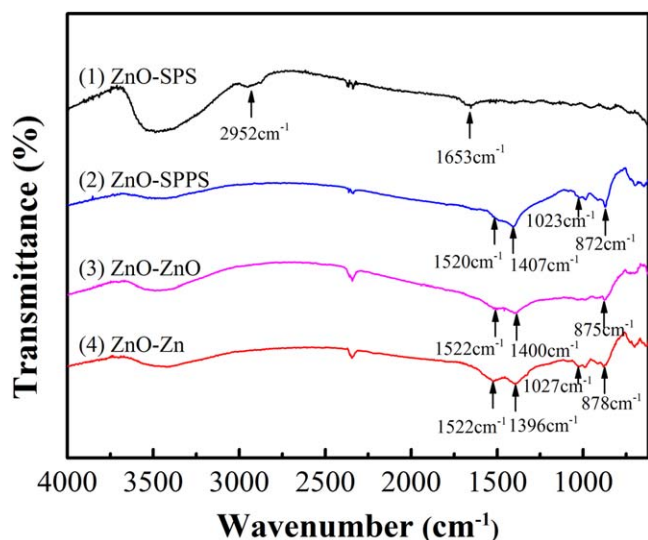
Figure 3. IR spectra of the ZnO coatings.

shift as compared to the ZnO–ZnO coating. The ZnO resulting from the thermal evaporation of zinc always exhibits favorable crystallinity [20]. It is worth noting that the addition of ZnO in the zinc acetate solution resulted in a remarkable peak shift for the coating when compared with the ZnO-SPPS coating. During the thermodynamic non-equilibrium process, the lattice oxygen in the ZnO lattice was prone to loss, resulting in certain lattice defects. For the ZnO–ZnO suspension spraying coating, a small amount of nano-ZnO particles are loaded on the basis of ZnO-SPPS. In the process of spraying, there was no chemical reaction and partial melting changed these uniformly dispersed nanoparticles. However, there is a certain lattice mismatch between the two sources of ZnO nanoparticles. Consequently, some lattice defects are formed in the as-sprayed ZnO coating. For the ZnO–Zn coating, low melting point Zn particles were introduced into the suspension. As an active metal, Zn could melt or even evaporate sharply in the plasma jet. The ZnO formed by oxidation on the surface of the Zn particles is similar to that of metal vapor reactive deposition coating, and its crystallinity is high, which reduces the diffraction peak deviation caused by defect ZnO.

A certain amount of organic binder in the as-sprayed coatings was recognized as detected by FTIR (figure 3). The broad peak located at $\sim$3400 cm^{-1} is attributed to the O–H stretching vibration of adsorbed water. The peaks located at 2952 and 1653 cm^{-1} are assigned to the –CH$_2$– stretching vibration and the –C=O– stretching vibration, respectively, both of which suggest the residue of PVP [45]. As for the samples derived from the acetate solution, the shoulder peak relating to the surface absorption water at 3400 cm^{-1} is shallow owing to to the less addition of PVP, whose nature is moisture absorption. The peaks between 2250 and 2500 cm^{-1} are an asymmetric stretching vibration of CO$_2$ in the atmosphere. The other three samples share similar curves with specific peaks at 1520 and 1400 cm^{-1}, which refer to the antisymmetric stretching vibration and symmetric stretching vibration of the carboxylate group separately [46]. The IR

peaks at $\sim$1020 and $\sim$870 cm^{-1} indicate the in-plane $-$CH$_3$ rock vibration and carbonate out-of-plane bending vibration, evidencing non-pyrolyzed precursors or intermediates [47]. The IR inspection suggests retained organics from the starting precursor solution, which act as a surfactant for the suspension and carboxylate or carbonate for the solution.

The as-sprayed coatings differ in topography (figure 4) and cross-sectional morphology (figure 5). The suspension coating (ZnO-SPS) exhibited a flat surface morphology and almost no pores were seen (figure 4(a-1)). The coating well retained the characteristics of the starting powder (figure 4(a-2) versus figure 1(b)), and few agglomerated spheres were recognized. The solution precursor coating (ZnO-SPPS) showed a uniform cauliflower-like topography with 5–20 μm aggregates (figure 4(b-1)), which were accumulated by the nanograins with a size of $\sim$100 nm (figure 4(b-2)). The coatings deposited using the hybrid liquid feedstock showed analogous structures. Both the ZnO–ZnO and the ZnO–Zn coatings exhibited a double-layered morphology comprising the typical clusters and fluffy top layer of ultrafine nanograins ($\sim$20 nm) (figures 4(c) and (d)).

To further characterize the spatial structure of the coatings, their fractured cross-sectional morphology was also examined (figure 5). The suspension coating showed a rarefied layer with an average thickness of $\sim$10 μm (figure 5(a)), and agglomerated particles with solidified cores were observed. The ZnO-SPPS coating showed tightly packed clusters with a dense bottom structure consisting of a well-molten powder. A certain amount of pores and vacancies were recognized at the root of each cluster. These structural features directly influence the photocatalytic activities of the coatings.

It is noted that the coatings made by the hybrid liquid spray route showed a porous skeleton-like structure. Both coatings were composed of ultrafine grains on their top layers. Micron-sized pores in between the agglomerates within the bottom zone and nano-sized pores within the top layer were recognized. The ZnO–Zn coating showed larger-sized pores and a tighter integral framework than the ZnO–ZnO coating.

To further elucidate the effect of the loading of the particles in the starting feedstock, the individual agglomerates realized within the coatings were evaluated (figure 6). It is suggested that the networking structure of the ZnO–ZnO coating (figures 6(a) and (b)) was generated from well-molten ZnO particles, which play the role of the binder. The binder offers the capability of assembling hollow microspheres [48] and the crashed shell was retained to form the porous skeleton, which caused the formation of the porous structure of the ZnO–Zn coating in this case. However, due to the unevenly distributed size of the Zn particles, large Zn particles over several micrometers survived and were embedded into the coating, even though the outer layer of the particles was presumably oxidized or affiliated by ultrafine ZnO grains (figures 6(c) and (d)). It has been reported that ZnO synthesized from thermal evaporation of Zn tends to bear an irregular shape [49]. In our case, the remaining Zn particles underwent subsequent melting, evaporation, and oxidation
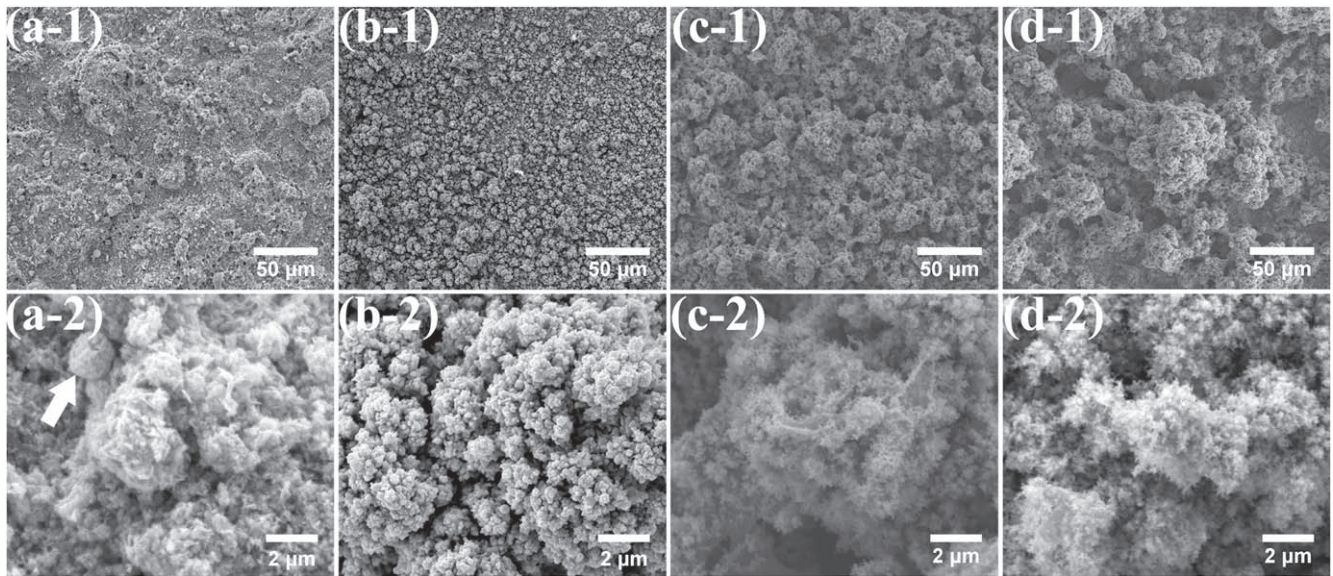
Figure 4. Surface morphology of the ZnO-SPS coating (the white arrow in (a-2) points to the typical aggregated ZnO particles) (a-1, a-2), the ZnO-SPPS coating (b-1, b-2), the ZnO–ZnO (c-1, c-2), and the ZnO–Zn coating (d-1, d-2).
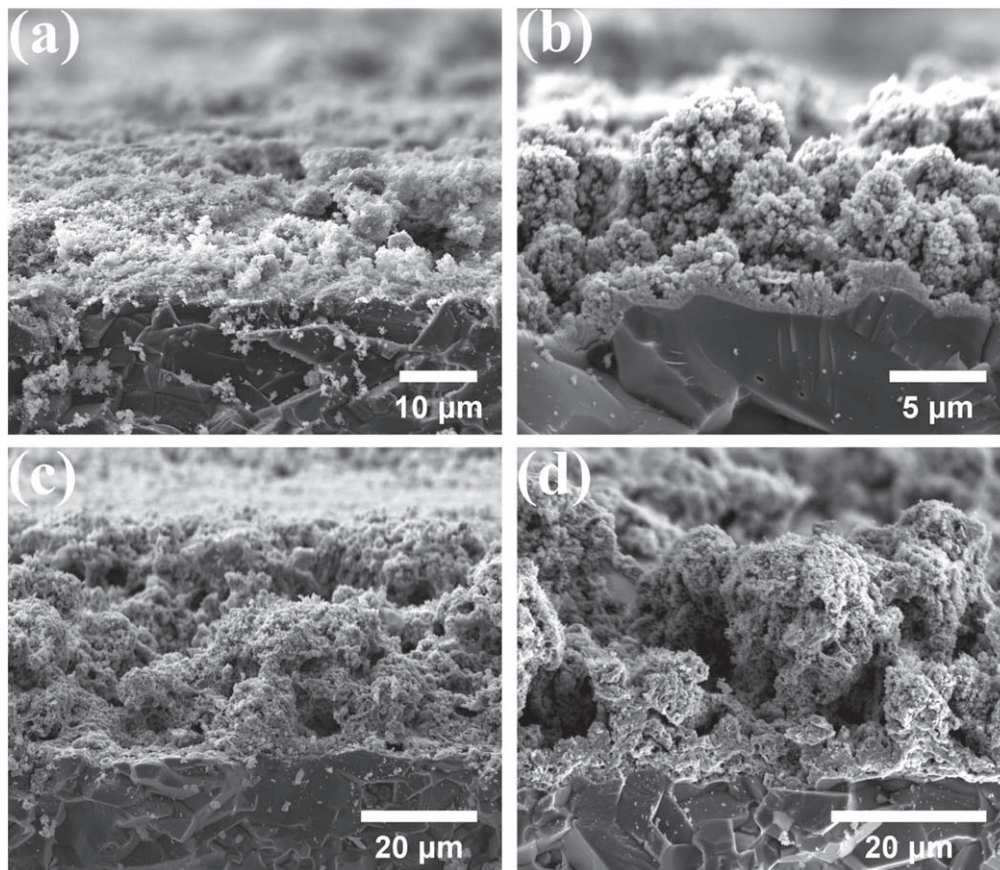

Figure 5. Fractured cross-sectional morphology of the as-sprayed ZnO coatings, (a) the ZnO-SPS coating, (b) the ZnO-SPPS coating, (c) ZnO–ZnO coating, and (d) the ZnO–Zn coating.

during the spraying, giving rise to the formation of large voids at the bottom layer of the coating.

The absorption curves acquired from UV–vis diffuse reflectance measurement showed more intensive adsorption of the coatings in UV range than in visible light range, and the

coating made from the Zn loaded precursor showed the best adsorption (figure 7(a)). It is known that absorption is closely related to surface roughness. The coating deposited using the ZnO powder tablet exhibited shifts in the absorption edge, which likely suggests variation in its band structure.
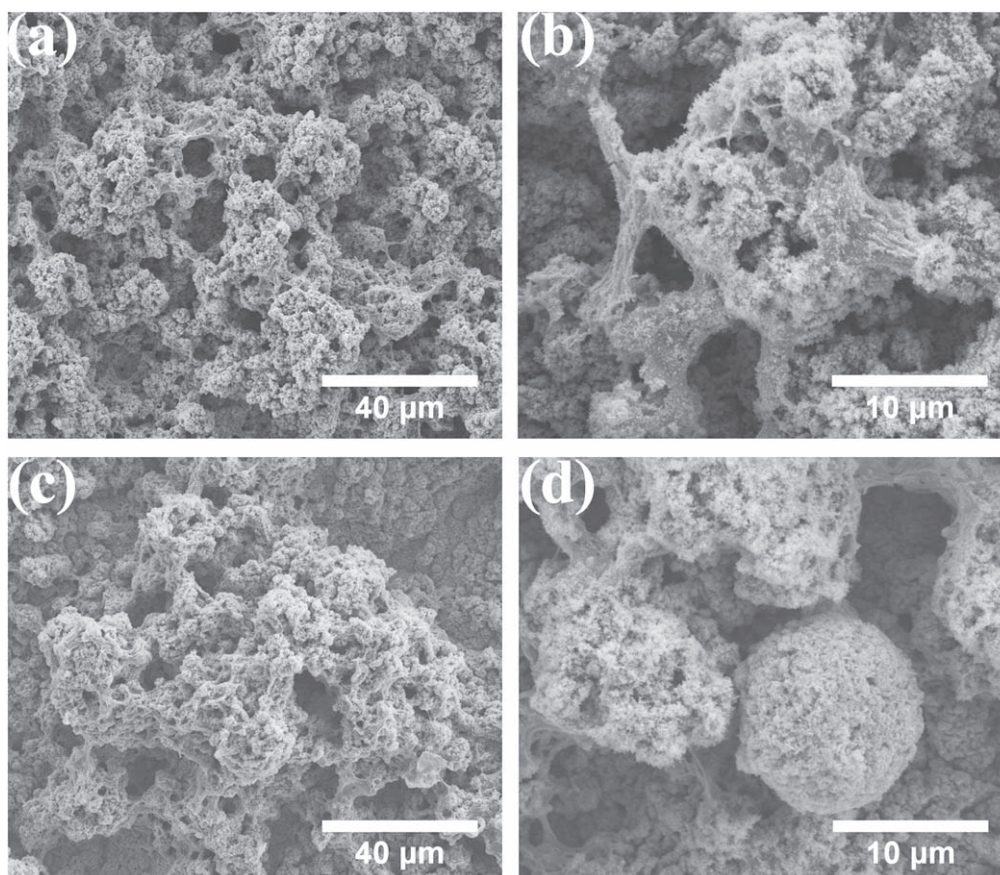
Figure 6. Typical morphology of the hybrid liquid sprayed ZnO–ZnO coating (a) and the hybrid liquid sprayed ZnO–Zn coating (c), (b) the porous skeleton structure of the ZnO–ZnO coating, and (d) the typical aggregated particles within the ZnO–Zn coating.

Calculation of the forbidden band gap (Eg) values using a Tauc plot indicated that all the coatings except the ZnO-SPS coating have a narrow band gap ranging from 3.068–3.093 eV. It has been claimed that the shift of the absorption curve suggests a crystal defect in ZnO–Zn coating [50]. These three coatings are mainly composed of ZnO *in situ* pyrolyzed with an ultrahigh temperature plasma torch and Ar-H$_2$ reducing atmosphere. During the SPPS process, the liquid droplets are usually subjected to evaporation, precipitation, and pyrolysis. Coatings with rich oxygen vacancies are easy to deposit due to the rapid heat-cooling process with reducing atmosphere [35, 51]. Additionally, the nano-sizing effect of semiconductors usually helps obtain an oxygen defect state [52]. As for the ZnO-SPS coating, it is likely that the initial particles are annealed during the spraying. The scanning electron microscopy images and the XRD spectra without peak shifting confirmed the calcined state of ZnO in the ZnO-SPS coating. As a result, the calcination-related defect-free coating gave rise to the band gap widening as shown in figure 7(b).

The photocatalytic performances of the ZnO coatings were assessed by measuring the degradation reaction of methylene blue under the irradiation of a UV light and an Xe lamp. All the coatings showed favorable degradation of the dye with a similar degradation rate of 80% after 6 h of UV illumination (figure 8(a)). The ZnO-SPPS coating performed the best among the coatings in terms of the degradation rate of

the dye, and further analysis based on the pseudo first order reaction kinetics [61] indicated the somewhat worse performance of the ZnO-SPS coatings (figure 8). Compared with the catalytic results reported in other literatures (table 2), the catalytic effect we obtained is of medium level.

To clarify the impact of the structural features of the coatings on their photocatalytic performances, their crystal defects and active surface states were examined by PL spectrometry conducted using a 325 nm He-Cd laser emission as the excitation source. All the coatings showed a sharp peak and a broad peak covering the visible light range (figure 9(a)). The UV peaks are located at 380 nm, which matches the band gap of ZnO (∼3.2 eV). This peak is ascribed to free-exciton emission and is referred to as near band edge (NBE) emission [52]. The NBE intensity of the ZnO–Zn coating sample was much higher than the other three, indicating its good crystallinity [62]. This feature can also be traced in its XRD pattern with respect to curve stiffness. Visible emission of ZnO is usually derived from crystal defects, which are referred to as deep level (DL) emission [63]. When comparing the emission intensity ratio of DL to NBE (inset of figure 9(a)), the ZnO–ZnO coating showed the highest ratio while the ZnO–Zn coating ranked the last. The DL/NBE value indicates the defect level of the coatings. There is no doubt that the well-crystallized ZnO–ZnO coating has rare crystal vacancies. The PL emission is the result of the recombination of excited electrons and holes, and the lower
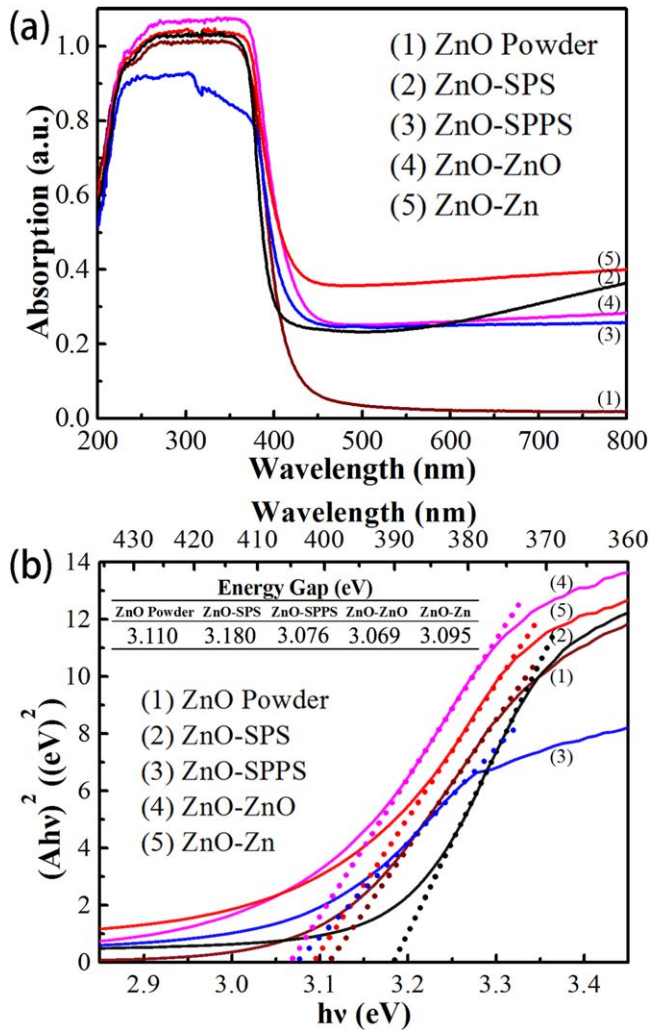
Figure 7. (a) UV–vis DRS of the ZnO coatings, and (b) the corresponding Tauc plots of the coatings (the inset in figure lists the calculated Eg values).

PL intensity indicates the lower recombination rate of photo-generated electrons and holes [64, 65]. As discussed previously, the photocatalytic reaction is proportional to the recombination rate of photo-generated electrons and holes. Hence, a higher PL intensity would bring about poorer photocatalytic performances [66]. The fluorescence of the ZnO-SPS and the ZnO-SPPS coatings exhibited a bias toward the orange light region (597–622 nm), while the hybrid sprayed ZnO–ZnO and ZnO–Zn coatings mainly responded to the green light region (492–577 nm). For further investigation into the discrepancy of the fluorescence distribution, peak separation was applied to analyze the specific emission peaks covering varied light regions.

According to the literature that has studied PL emission, the actual curves were separated into five peaks by a Gaussian approximation (figures 9(b)–(e)). There is a good match between the cumulative curves and the corresponding tested curves. The five peaks are referred to as A–E: A (380 nm wavelength) and B (400 nm wavelength) were in the UV region, C (510 nm), D (560 nm) and E (650 nm) were in accordance with the green, green-yellow, and orange-red emissions, respectively. The peak located at 380 nm (A) represents the NBE emission [67–71] and the adjoining peak (B) was reported to be relevant to the electron transition from the bottom of the conduction band to the Zn vacancy level (CB) $\rightarrow$ V$_{Zn}$ [72]. Green emission is the most commonly observed defect emission in nanostructured ZnO, and it is often attributed to a singly ionized oxygen vacancy (V_0^+) [73, 74]. A non-radiative electron captured from CB by V_0^+ leads to an unstable state that recombines with a photoexcited hole in the VB [74]. Similarly, a doubly charged oxygen vacancy (V_0^{++}) state undergoes radiative recombination with a CB electron to yield PL of approximately 2.20 eV (564 nm) [75]. More importantly, the grain boundary-induced depletion regions lead to the formation of a deeply trapped state. Besides, the orange-red emission (643 nm) has been assigned to excess (surface) oxygen in the work of Studenikin *et al* [23].

The emission intensity of each fitting curve was recorded (figure 9(f)). Unlike the peaks A and B, peak C of the ZnO-SPS and the ZnO-SPPS coatings is negligible as compared to the ZnO–ZnO and the ZnO–Zn coatings. The other peaks share similar trends from peak D to peak E (figure 9(f)). It is noted that the ZnO–ZnO coating has higher green emission (C, D) than the ZnO–Zn coating, suggesting its more severe oxygen poor state. It is clear that the ZnO/Zn loaded precursor solution as the starting feedstock resulted in ZnO coatings with enhanced PL emission in the green light region, which indicates altered oxygen defects in the coatings as compared to traditional SPS/SPPS coatings.

During the suspension plasma spraying, the coatings obtained the evenly distributed grains from the pre-synthesized powder. The solid ZnO/Zn particles underwent limited heat input and physical reaction due predominately to the solvent evaporation. This well explains the good crystallinity and scarce vacancies of the ZnO-SPS coatings. Owing to the broad band gap, strong oxidation-reduction potential is anticipated in photocatalytic reactions. As for the solution precursor sprayed coatings, the typical oxygen-deficient feature would give rise to crystal lattice disorder and donor defect in the electron band. However, the coarsened ZnO grains also likely means an elongated depletion layer, in turn hindering the transmission of photo-generated carriers from internal to boundary, and the photocatalytic reactions would be weakened consequently.

After the loading of the solid particles into the solution precursor, the coatings exhibited dominant typical SPPS coating features like the nanostructures. The nano-sized ZnO particles loaded in the starting liquid provided an adhering skeleton for the coatings, rather than promoting crystalline orientation for zinc acetate pyrolysis during the *in situ* reactions. Consequently, the hybrid architecture brought about the possibility of forming crystal defects (grain boundary), which is suggested by the remarkable shifting of the XRD peaks and the absorption edge in the UV–vis DRS. Furthermore, the intense DL emission in the PL spectra verified the existence of mass defects, probably the oxygen vacancies V_0^+ and V_0^{++} in the ZnO–ZnO coatings. The loading of the Zn particles in the starting liquid precursor enhanced the crystallization of
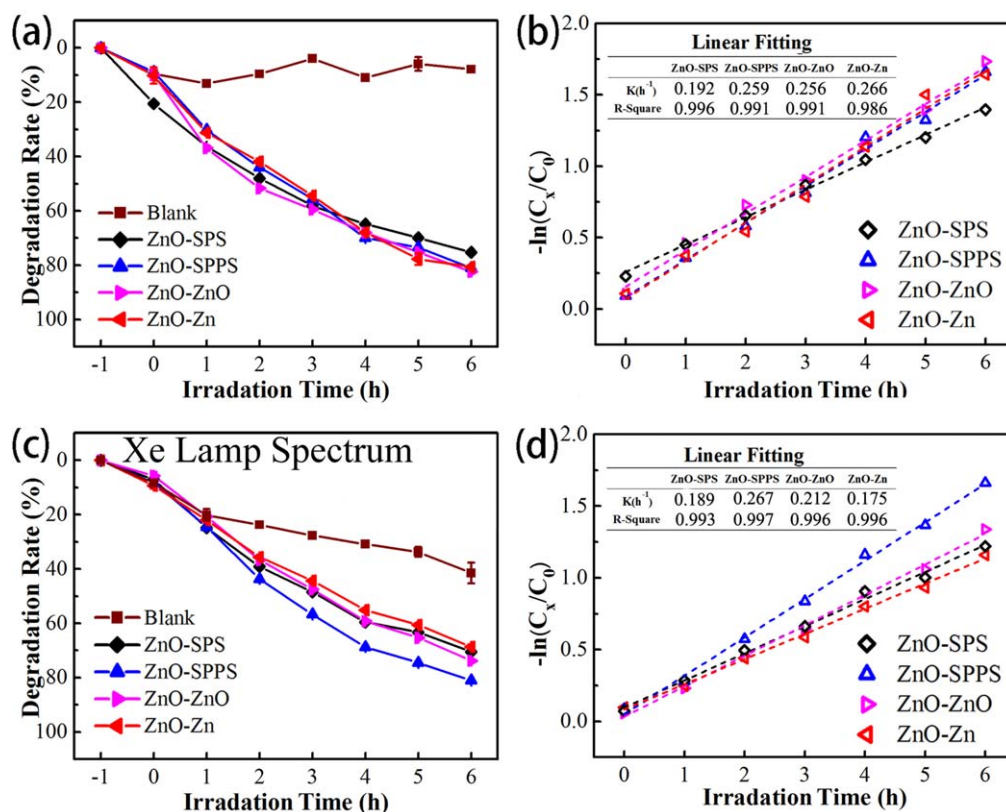
Figure 8. Degradation rate of methylene blue in the presence of the ZnO coatings under the irradiation of a UV light (a) and an Xe lamp (b); and the plots of $-\ln(C_x/C_0)$ versus irradiation time are also shown for the coatings illuminated under a UV light (c) and an Xe lamp (d), the insets list the linear fitting results.

Table 2. Comparison of the photocatalytic properties of the ZnO films.

Materials	Methods	Degradation	References
ZnO film on conducting glass	Electro-spray	86.5%, 120 min, high concentration MB; 96.0%, 120 min, low concentration MB	[53]
ZnO nanocomposite coating film	Electrophoreted	58%, 180 min, removal of 2-chlorophenol	[54]
ZnO-coated multi-walled carbon nanotubes	Sol process	97%, 30 min, removal methyl orange	[55]
ZnO thin films	Spin coating method	95%, 270 min, removal rhodamine-B	[56]
ZnO thin films	Sol-gel dip-coating method	74%, 240 min, removal MB	[57]
TiO2-ZnO (5%) thin films on the surface of polycarbonate	Dip-coating	87%, 24 h, removal MB and methyl stearate	[58]
ZnO thin film	Slow hydrolysis method	76%, 180 min, removal nitrophenols	[59]
Cu doped ZnO thin films	Sol-gel dip-method	95%, 480 min, removal MB	[60]
ZnO coating	Thermal spraying	80%, 360 min, removal MB	Our work

the major phases in the coatings through thermal oxidation of Zn, which occurred during the spraying. This eventually decreased the DL/NBE ratio. The unevenly distributed Zn particles pre-dispersed in the precursor had two typical particle sizes: 100 nm and several micrometers. The former helped construct a porous skeleton with the assistance of organic additives and the latter were partially oxidized or evaporated by successive heating. The tuned nanostructures and structural defects triggered by the ZnO/Zn loading in the liquid precursor already showed a significant impact on the photocatalytic activities of the coatings. This novel technical route provides insight into the design and thermal spray fabrication of nanostructured functional coatings for various applications.

4. Conclusions

ZnO coatings with nanograins and peculiar bimodal structures were efficiently one-step fabricated by a liquid
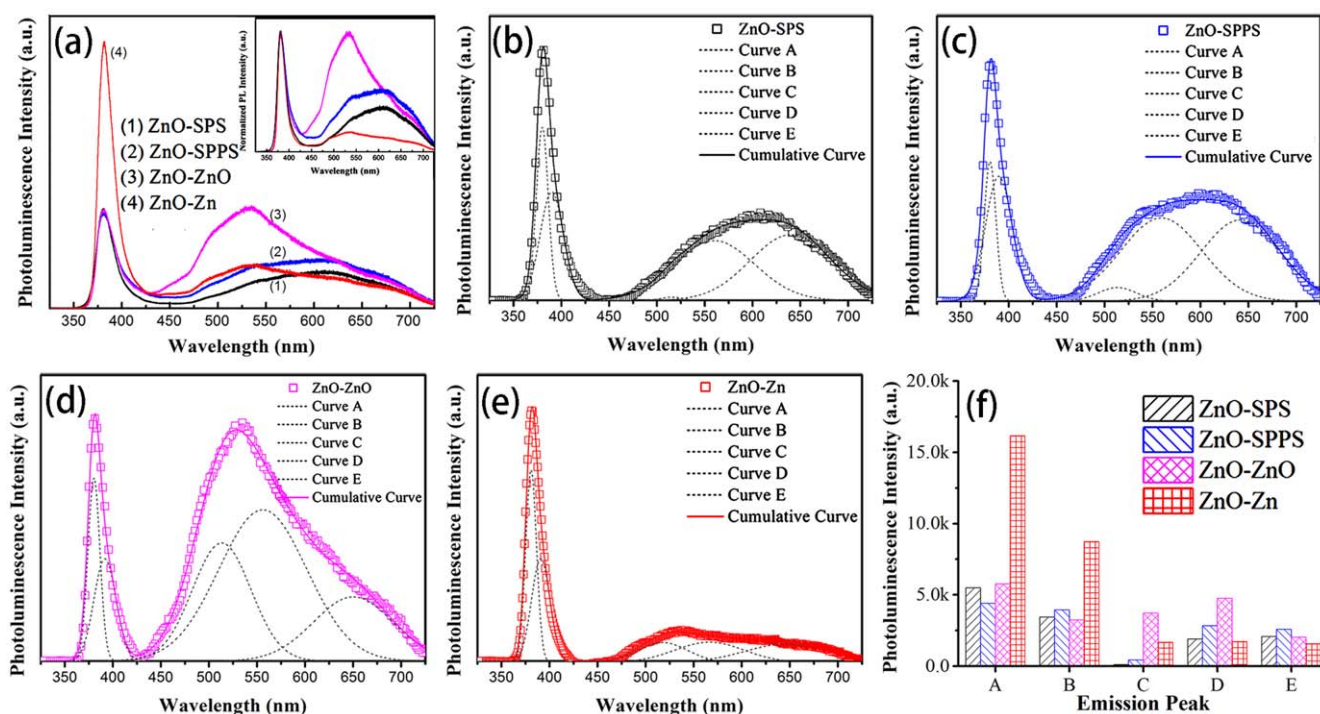
Figure 9. Room temperature PL spectra of the coatings, (a) PL spectrum (the graph in the inset shows the normalized spectra), (b)–(e) corresponding deconvoluted peaks, and (f) PL peak intensity.

precursor plasma spray. The addition of solid ZnO/Zn particles in the starting precursor solution resulted in the formation of a skeleton architecture and the modified surface state of the coatings. The hybrid liquid sprayed ZnO coatings exhibited a double-layered porous structure with ultrafine nanograins being retained at the uppermost layer. Compared to the traditional suspension or solution precursor sprayed coatings, these coatings showed a remarkably enhanced optical response and corresponding photocatalytic activities under UV and simulated sunlight irradiation. The promoted photocatalytic performances were revealed to be related to oxygen defects existing in the coatings as triggered by the ZnO or Zn particles pre-loaded in the starting suspension. The results provide insight into tailoring the structures of liquid thermal sprayed coatings by adjusting the starting liquid feedstock through mixing micron-/nano-sized particles.

ORCID iDs

Yi Liu ⬤ https://orcid.org/0000-0003-3489-0841

References

[1] Djurišić A B, Chen X, Leung Y H and Man Ching Ng A 2012 ZnO nanostructures: growth, properties and applications *J. Mater. Chem.* **22** 6526–35

[2] Janotti A and Van de Walle C G 2009 Fundamentals of zinc oxide as a semiconductor *Rep. Prog. Phys.* **72** 126501

[3] Chougule M A, Sen S and Patil V B 2012 Fabrication of nanostructured ZnO thin film sensor for NO_2 monitoring, *Ceram. Int.* **38** 2685–92

[4] Zayer N K, Greef R, Rogers K, Grellier A J C and Pannell C N 1999 *In situ* monitoring of sputtered zinc oxide films for piezoelectric transducers *Thin Solid Films* **352** 179–84

[5] Kumar V, Singh R G, Singh F and Purohit L P 2012 Highly transparent and conducting boron doped zinc oxide films for window of dye sensitized solar cell applications *J. Alloys Compd.* **544** 120–4

[6] Kim S, Moon H, Gupta D, Yoo S and Choi Y K 2009 Resistive switching characteristics of sol-gel zinc oxide films for flexible memory applications *IEEE Trans. Electron Devices* **56** 696–9

[7] Shin P K, Aya Y, Ikegami T and Ebihara K 2008 Application of pulsed laser deposited zinc oxide films to thin film transistor device *Thin Solid Films* **516** 3767–71

[8] Zhang Y, Bian T, Gu J, Zheng X and Li Z 2018 Controllable ZnO architectures with the assistance of ethanolamine and their application for removing divalent heavy metals (Cu, Pb, Ni) from water *New J. Chem.* **42** 3356–62

[9] Zhang Y, Chen Z, Liu S and Xu Y J 2013 Size effect induced activity enhancement and anti-photocorrosion of reduced graphene oxide/ZnO composites for degradation of organic dyes and reduction of Cr(VI) in water *Appl. Catal.* B **140–1** 598–607

[10] Ramirez-Canon A, Medina-Llamas M, Vezzoli M and Mattia D 2018 Multiscale design of ZnO nanostructured photocatalysts *Phys. Chem. Chem. Phys.* **20** 6648–56

[11] Portillo-Vélez N S and Bizarro M 2016 Sprayed pyrolyzed ZnO films with nanoflake and nanorod morphologies and their photocatalytic activity *J. Nanomater.* 1–11

[12] Al-Sabahi J, Bora T, Al-Abri M and Dutta J 2016 Controlled defects of zinc oxide nanorods for efficient visible light photocatalytic degradation of phenol *Materials (Basel).* **9** 238

[13] Ali A M, Emanuelsson E A C and Patterson D A 2010 Photocatalysis with nanostructured zinc oxide thin films: the relationship between morphology and photocatalytic activity under oxygen limited and oxygen rich conditions and evidence for a Mars Van Krevelen mechanism *Appl. Catal.* B **97** 168–81

[14] Carvalho K T G, Fidelis S C, Lopes O F and Ribeiro, C 2015 Effect of processing variables on the photocatalytic properties of Zno thin films prepared using the polymeric precursor method *Ceram. Int.* **41** 10587–94

[15] Srikanth B, Goutham R, Badri Narayan R, Ramprasath A, Gopinath K P and Sankaranarayanan A R 2017 Recent advancements in supporting materials for immobilised photocatalytic applications in waste water treatment *J. Environ. Manage.* **200** 60–78

[16] Tong Y, Liu Y, Dong L, Zhao D, Zhang J, Lu Y, Shen D and Fan X 2006 Growth of ZnO nanostructures with different morphologies by using hydrothermal technique *J. Phys. Chem.* B **110** 20263–7

[17] Amin G, Asif M H, Zainelabdin A, Zaman S, Nur O and Willander M 2011 Influence of pH, precursor concentration, growth time, and temperature on the morphology of ZnO nanostructures grown by the hydrothermal method *J. Nanomater.* **2011** 1–9

[18] Xu L, Hu Y L, Pelligra C, Chen C H, Jin L, Huang H, Sithambaram S, Aindow M, Joesten R and Suib S L 2009 ZnO with different morphologies synthesized by solvothermal methods for enhanced photocatalytic activity *Chem. Mater.* **21** 2875–85

[19] Yang J L, An S J, Il Park W, Yi G C and Choi W 2004 Photocatalysis using ZnO thin films and nanoneedles grown by metal-organic chemical vapor deposition *Adv. Mater.* **16** 1661–4

[20] Fouad O A, Ismail A A, Zaki Z I and Mohamed R M 2006 Zinc oxide thin films prepared by thermal evaporation deposition and its photocatalytic activity *Appl. Catal.* B **62** 144–9

[21] Rogé V, Bahlawane N, Lamblin G, Fechete I, Garin F, Dinia A and Lenoble D 2015 Improvement of the photocatalytic degradation property of atomic layer deposited ZnO thin films: the interplay between film properties and functional performances *J. Mater. Chem.* A **3** 11453–61

[22] Hayat K, Gondal M A, Khaled M M, Ahmed S and Shemsi A M 2011 Nano ZnO synthesis by modified sol gel method and its application in heterogeneous photocatalytic removal of phenol from water *Appl. Catal.* A **393** 122–9

[23] Studenikin S A, Golego N and Cocivera M 1998 Fabrication of green and orange photoluminescent, undoped ZnO films using spray pyrolysis *J. Appl. Phys.* **84** 2287–94

[24] Zhang C, Debliquy M and Liao H 2010 Deposition and microstructure characterization of atmospheric plasma-sprayed ZnO coatings for NO$_2$ detection *Appl. Surf. Sci.* **256** 5905–10

[25] Navidpour A H, Kalantari Y, Salehi M, Salimijazi H R, Amirnasr M, Rismanchian M and Azarpour Siahkali M 2017 Plasma-sprayed photocatalytic zinc oxide coatings *J. Therm. Spray Technol.* **26** 717–27

[26] Lin H F, Liao S C and Hung S W 2005 The DC thermal plasma synthesis of ZnO nanoparticles for visible-light photocatalyst *J. Photochem. Photobiol.* A **174** 82–7

[27] Pawlowski L 2009 Suspension and solution thermal spray coatings *Surf. Coatings Technol.* **203** 2807–29

[28] Killinger A, Gadow R, Mauer G, Guignard A, Vaen R and Stöver D 2011 Review of new developments in suspension and solution precursor thermal spray processes *J. Therm. Spray Technol.* **20** 677–95

[29] Fauchais P and Montavon G 2010 Latest developments in suspension and liquid precursor thermal spraying *J. Therm. Spray Technol.* **19** 226–39

[30] Sanpo N, Wang J, Ang A S M and Berndt C C 2013 Influence of the different organic chelating agents on the topography, physical properties and phase of SPPS-deposited spinel ferrite splats *Appl. Surf. Sci.* **284** 171–8

[31] Bertolissi G, Chazelas C, Bolelli G, Lusvarghi L, Vardelle M and Vardelle A 2012 Engineering the microstructure of solution precursor plasma-sprayed coatings *J. Therm. Spray Technol.* **21** 1148–62

[32] Chen D, Jordan E H and Gell M 2010 The solution precursor plasma spray coatings: influence of solvent type *Plasma Chem. Plasma Process.* **30** 111–9

[33] Chen D, Jordan E H and Gell M 2008 Effect of solution concentration on splat formation and coating microstructure using the solution precursor plasma spray process *Surf. Coatings Technol.* **202** 2132–8

[34] Xie L, Ma X, Ozturk A, Jordan E H, Padture N P, Cetegen B M, Xiao D T and Gell M 2004 Processing parameter effects on solution precursor plasma spray process spray patterns *Surf. Coatings Technol.* **183** 51–61

[35] Zhang C, Geng X, Liao H, Li C J and Debliquy M 2017 Room-temperature nitrogen-dioxide sensors based on ZnO$_{1-x}$ coatings deposited by solution precursor plasma spray *Sensors Actuators* B **242** 102–11

[36] Zhang C, Geng X, Li J, Luo Y and Lu P 2017 Role of oxygen vacancy in tuning of optical, electrical and NO$_2$ sensing properties of ZnO$_{1-X}$ coatings at room temperature *Sensors Actuators* B **248** 886–93

[37] Zhang C, Geng X, Li H, He P J, Planche M P, Liao H, Olivier M G and Debliquy M 2015 Microstructure and gas sensing properties of solution precursor plasma-sprayed zinc oxide coatings *Mater. Res. Bull.* **63** 67–71

[38] Yu Z, Moussa H, Ma Y, Liu M, Chouchene B and Schneider R 2019 Oxygen-defective ZnO films with various nanostructures prepared via a rapid one-step process and corresponding photocatalytic degradation applications *J. Colloid Interface Sci.* **534** 637–48

[39] Yu Z X, Ma Y Z, Zhao Y L, Huang J B, Wang W Z, Moliere M and Liao H L 2017 Effect of precursor solutions on ZnO film via solution precursor plasma spray and corresponding gas sensing performances *Appl. Surf. Sci.* **412** 683–9

[40] Yu Z, Moussa H, Liu M, Chouchene B, Schneider R, Wang W, Moliere M and Liao H 2018 Tunable morphologies of ZnO films via the solution precursor plasma spray process for improved photocatalytic degradation performance *Appl. Surf. Sci.* **455** 970–9

[41] Huang J, Wang X, Gong Y, Liu Y, Zhou P, Suo X, Zeng D and Li H 2017 Construction of WO$_3$ coatings with micro-nano hybrid structures by liquid precursor flame spray for enhanced sensing performances to sub-ppm ozone *Mater. Lett.* **205** 106–9

[42] Wu Q, Huang J and Li H 2015 Deposition of porous nano-WO$_3$ coatings with tunable grain shapes by liquid plasma spraying for gas-sensing applications *Mater. Lett.* **141** 100–3

[43] Zhai M, Liu Y, Huang J, Wang Y, Chen K, Fu Y and Li H 2018 Efficient suspension plasma spray fabrication of black titanium dioxide coatings with visible light absorption performances *Ceram. Int.* **45** 930–5

[44] Física S M D, México A C, Morales E, Mora S, Pal E, Morales A E, Mora E S and Pal U 2007 Use of diffuse reflectance spectroscopy for optical characterization of un-supported nanostructures *Rev. Mex. Fis.* **53** 18–22

[45] Wei S F, Lian J S and Jiang Q 2009 Controlling growth of ZnO rods by polyvinylpyrrolidone (PVP) and their optical properties *Appl. Surf. Sci.* **255** 6978–84

[46] Adamopoulos G, Bashir A, Gillin W P, Georgakopoulos S, Shkunov M, Baklar M A, Stingelin N, Bradley D D C and Anthopoulos T D 2011 Structural and electrical characterization of ZnO films grown by spray pyrolysis and their application in thin-film transistors *Adv. Funct. Mater.* **21** 525–31

[47] Song Y, Yang Y and Liang H 2009 ZnO nanoparticles prepared by thermal decomposition of batch supercritical antisolvent processed zinc acetate *J. Chem. Eng. Jpn.* **42** 117–25

[48] Ren K, Liu Y, He X and Li H 2015 suspension plasma spray fabrication of nanocrystalline titania hollow microspheres for photocatalytic applications *J. Therm. Spray Technol.* **24** 1213–20

[49] Gupta R K, Shridhar N and Katiyar M 2002 Structure of ZnO films prepared by oxidation of metallic zinc *Mater. Sci. Semicond. Process.* **5** 11–5

[50] Wang J, Wang Z, Huang B, Ma Y, Liu Y, Qin X, Zhang X and Dai Y 2012 Oxygen vacancy induced band-gap narrowing and enhanced visible light photocatalytic activity of ZnO *ACS Appl. Mater. Interfaces* **4** 4024–30

[51] Xu P, Coyle T W, Pershin L and Mostaghimi J 2019 Fabrication of superhydrophobic ceramic coatings via solution precursor plasma spray under atmospheric and low-pressure conditions *J. Therm. Spray Technol.* **28** 242–54

[52] Motaung D E, Makgwane P R and Ray S S 2015 Induced ferromagnetic and gas sensing properties in ZnO-nanostructures by altering defect concentration of oxygen and zinc vacancies *Mater. Lett.* **139** 475–9

[53] Valenzuela L, Iglesias A, Faraldos M, Bahamonde A and Rosal R 2019 Antimicrobial surfaces with self-cleaning properties functionalized by photocatalytic ZnO electrosprayed coatings *J. Hazard. Mater.* **369** 665–73

[54] Abdel Aal A, Barakat M A and Mohamed R M 2008 Electrophoreted Zn–TiO$_2$–ZnO nanocomposite coating films for photocatalytic degradation of 2-chlorophenol *Appl. Surf. Sci.* **254** 4577–83

[55] Zhu L-P, Liao G-H, Huang W-Y, Ma L-L, Yang Y, Yu Y and Fu S-Y 2009 Preparation, characterization and photocatalytic properties of ZnO-coated multi-walled carbon nanotubes *Mater. Sci. Eng.: B* **163** 194–8

[56] Kaviyarasu K *et al* 2017 Elucidation of photocatalysis, photoluminescence and antibacterial studies of ZnO thin films by spin coating method *J. Photochem. Photobiol. B* **173** 466–75

[57] Thongsuriwong K, Amornpitoksuk P and Suwanboon S 2013 Structure, morphology, photocatalytic and antibacterial activities of ZnO thin films prepared by sol–gel dip-coating method *Adv. Powder Technol.* **24** 275–80

[58] Fateh R, Dillert R and Bahnemann D 2014 Self-cleaning properties, mechanical stability, and adhesion strength of transparent photocatalytic TiO$_2$–ZnO coatings on polycarbonate *ACS Appl. Mater. Inter.* **6** 2270–8

[59] Qamar M T, Aslam M, Ismail I M I, Salah N and Hameed A 2015 Synthesis, characterization, and sunlight mediated photocatalytic activity of CuO coated ZnO for the removal of nitrophenols *ACS Appl. Mater. Inter.* **7** 8757–69

[60] Jongnavakit P, Amornpitoksuk P, Suwanboon S and Ndiege N 2012 Preparation and photocatalytic activity of Cu-doped ZnO thin films prepared by the sol–gel method *Appl. Surf. Sci.* **258** 8192–8

[61] Ismail L F M, Emara M M, El-Moselhy M M, Maziad N A and Hussein O K 2014 Silica coating and photocatalytic activities of ZnO nanoparticles: effect of operational parameters and kinetic study *Spectrochim. Acta* A **131** 158–68

[62] Jin B J, Im S and Lee S Y 2000 Violet and UV luminescence emitted from ZnO thin films grown on sapphire by pulsed laser deposition *Thin Solid Films* **366** 107–10

[63] Li D, Leung Y H, Djurišić A B, Liu Z T, Xie M H, Shi S L, Xu S J and Chan W K 2004 Different origins of visible luminescence in ZnO nanostructures fabricated by the chemical and evaporation methods *Appl. Phys. Lett.* **85** 1601–3

[64] Wang F, Liang L, Shi L, Liu M and Sun J 2014 CO$_2$-assisted synthesis of mesoporous carbon/C-coped ZnO composites for enhanced photocatalytic performance under visible light *Dalton Trans.* **43** 16441–9

[65] He J, Luo Q, Cai Q Z, Li X W and Zhang D Q 2011 Microstructure and photocatalytic properties of WO$_3$/TiO$_2$ composite films by plasma electrolytic oxidation *Mater. Chem. Phys.* **129** 242–8

[66] Ruiz Peralta M D L, Pal U and Zeferino R S 2012 Photoluminescence (PL) quenching and enhanced photocatalytic activity of Au-decorated ZnO nanorods fabricated through microwave-assisted chemical synthesis *ACS Appl. Mater. Interfaces* **4** 4807–16

[67] Ahsanulhaq Q, Kim J H, Kim J H and Hahn Y B 2010 Seedless pattern growth of quasi-aligned ZnO nanorod arrays on cover glass substrates in solution *Nanoscale Res. Lett.* **5** 669–74

[68] Bougrine A, El Hichou A, Addou M, Ebothé J, Kachouane A and Troyon M 2003 Structural, optical and cathodoluminescence characteristics of undoped and tin-doped ZnO thin films prepared by spray pyrolysis *Mater. Chem. Phys.* **80** 438–45

[69] Cho S, Ma J, Kim Y, Sun Y, Wong G K L and Ketterson J B 1999 Photoluminescence and ultraviolet lasing of polycrystalline ZnO thin films prepared by the oxidation of the metallic Zn *Appl. Phys. Lett.* **75** 2761–3

[70] Van Dijken A, Meulenkamp E A, Vanmaekelbergh D and Meijerink A 2000 Luminescence of nanocrystalline ZnO particles: the mechanism of the ultraviolet and visible emission *J. Lumin.* **87** 454–6

[71] Wang M, Cheng X and Yang J 2009 Controlled visible photoluminescence of ZnO thin films prepared by RF magnetron sputtering *Appl. Phys.* A **96** 783–7

[72] Jeong S H, Kim B S and Lee B T 2003 Photoluminescence dependence of ZnO films grown on Si(100) by radio-frequency magnetron sputtering on the growth ambient *Appl. Phys. Lett.* **82** 2625–7

[73] Vanheusden K, Seager C H, Warren W L, Tallant D R, Caruso J, Hampden-Smith M J and Kodas T T 1997 Green photoluminescence efficiency and free-carrier density in ZnO phosphor powders prepared by spray pyrolysis *J. Lumin.* **75** 11–6

[74] Vanheusden K, Warren W L, Seager C H, Tallant D R, Voigt J A and Gnade B E 1996 Mechanisms behind green photoluminescence in ZnO phosphor powders *J. Appl. Phys.* **79** 7983–90

[75] Ye J D *et al* 2005 Correlation between green luminescence and morphology evolution of ZnO films *Appl. Phys.* A **81** 759–62